

Efficient and stable perovskite-silicon tandem solar cells through contact displacement by MgF_x

Jiang Liu^{1*}, Michele De Bastiani¹, Erkan Aydin¹, George T. Harrison¹, Yajun Gao¹, Rakesh R. Pradhan¹, Mathan K. Eswaran¹, Mukunda Mandal², Wenbo Yan¹, Akmaral Seitkhan¹, Maxime Babics¹, Anand S. Subbiah¹, Esma Ugur¹, Fuzong Xu¹, Lujia Xu¹, Mingcong Wang¹, Atteq ur Rehman¹, Arsalan Razzaq¹, Jingxuan Kang¹, Randi Azmi¹, Ahmed Ali Said¹, Furkan H. Isikgor¹, Thomas G. Allen¹, Denis Andrienko², Udo Schwingenschlögl¹, Frédéric Laquai¹, Stefaan De Wolf^{1*}

¹KAUST Solar Center, Physical Sciences and Engineering Division, King Abdullah University of Science and Technology (KAUST), Thuwal 23955-6900, Kingdom of Saudi Arabia. ²Max Planck Institute for Polymer Research, 55128 Mainz, Germany.

*Corresponding author. Email: jiang.liu@kaust.edu.sa (J.L.); stefaan.dewolf@kaust.edu.sa (S.D.W.)

The performance of perovskite solar cells with inverted polarity (*p-i-n*) is still limited by recombination at their electron extraction interface, which also lowers the power conversion efficiency (PCE) of *p-i-n* perovskite-silicon tandem solar cells. A ~1 nm thick MgF_x interlayer at the perovskite/ C_{60} interface through thermal evaporation favorably adjusts the surface energy of the perovskite layer, facilitating efficient electron extraction, and displaces C_{60} from the perovskite surface to mitigate nonradiative recombination. These effects enable a champion V_{oc} of 1.92 volts, an improved fill factor of 80.7%, and an independently certified stabilized PCE of 29.3% for a ~1 cm^2 monolithic perovskite-silicon tandem solar cell. The tandem retained ~95% of its initial performance following damp-heat testing (85 Celsius at 85% relative humidity) for > 1000 hours.

Integrating high-performance wide-bandgap perovskite solar cells onto silicon solar cells can lead to very high power conversion efficiencies (PCEs) by minimizing carrier-thermalization losses (1–6). Although initial research explored *n-i-p* tandems, recent works have focused on the *p-i-n* configuration, in which the *n*-type electron-collecting contact faces sunward (7–9), and on improving performance through device optics and optimizing perovskite composition (10–15). More recently, attention turned to the interface between the perovskite and the hole transport layer (HTL) to reduce voltage losses. Approaches include molecular passivation of NiO_x (16, 17) and the use of self-assembled monolayers (SAMs) such as 2PACz and Me-4PACz, anchored on oxides, to reduce V_{oc} losses (18, 19).

Despite this progress, state-of-art PSCs, especially those incorporating wider-bandgap perovskites (e.g., ~1.68 eV as frequently used for tandem applications), have an undesirably large V_{oc} deficit when compared to the theoretical radiative limit. This problem mainly stems from substantial charge carrier recombination and an energy level mismatch at the perovskite interface with the electron transport layer (ETL) (20–22), which most commonly consists of evaporated C_{60} . Inserting an ultrathin LiF layer at the perovskite/ C_{60} interface alleviates this issue to a certain extent, yet this

may result in reduced device stability, usually attributed to the deliquescent behavior and high ion diffusivity of Li salts (19, 23–25). Two-dimensional (2D) perovskites and some fullerene derivatives prepared by solution processes have been previously used to passivate the perovskite/ C_{60} rear interface in single-junction *p-i-n* PSCs (26, 27). However, in the *p-i-n* tandem configuration, the perovskite/ C_{60} interface faces sunwards, which demands interfacial layers with a high transparency, high stability and good thickness control. To this end, we systematically investigated alternative evaporated metal fluorides (such as NaF, CaF_x , and MgF_x) as interlayer at the perovskite/ C_{60} interface. We demonstrated that the charge transport and recombination interfaces could be carefully tuned with MgF_x interlayers, enabling a certified stabilized PCE of 29.3%.

We fabricated monolithic perovskite-silicon tandem solar cells from silicon heterojunction (SHJ) bottom cells using crystalline silicon (c-Si) wafers with double-side texture (Fig. 1A) to reduce the front reflection and improve light trapping in our devices (8, 16). We verified the ultrathin nature of the fluoride-based interlayers, inserted at the electron-selective top contact, with cross-sectional high-resolution scanning transmission electron microscopy (HR-STEM, Fig. 1B and figs. S1 and S2). The magnified STEM

images and energy-dispersive X-ray (EDX) spectroscopy mapping clearly outline the perovskite/MgF_x/C₆₀/SnO₂/IZO top contact structure, identifying the presence of a ~15 nm C₆₀ layer and a ~20 nm SnO₂ layer. The latter acts as a buffer against damage from sputtering of the indium zinc oxide (IZO) transparent top electrode (28). We note that after perovskite deposition, all subsequently deposited films were obtained by vapor deposition techniques that yield highly accurate and reproducible layer thicknesses. For instance, because the fluoride-based film is thermally evaporated, the resulting interlayer is highly uniform in thickness, less affected by the surface roughness of the underlying perovskite, contrasting with typical solution-processed interlayers (27).

We investigated the energy-level alignment of our perovskite layers with LiF, NaF, CaF_x and MgF_x overlayers by ultraviolet photoemission spectroscopy (UPS) and low-energy inverse photoemission spectroscopy (LE-IPES) for occupied and unoccupied states, respectively. As shown in Fig. 1C, the work function (*WF*) of the bare perovskite is ~4.97 eV. By coating the perovskite with a thin fluoride-based layer, the *WF* systematically shifts toward smaller values. Both MgF_x and CaF_x caused a larger *WF* shift than LiF and NaF did (Fig. 1C and fig. S3). With the presence of metal fluoride interlayers, the valence band maximum (*VBM*) of the perovskite, determined with a Gaussian fitting method (29), was lowered relative to its Fermi level (*E_F*), implying that the metal fluorides caused a downward band bending at the perovskite interface that favored electron extraction.

Kelvin probe force microscopy (KPFM) measurements, conducted in an ambient environment, confirmed the trend of the UPS results (fig. S4) (30), that is, the MgF_x and CaF_x samples displayed a larger *WF* shift compared to LiF and NaF ones (fig. S5). To further evaluate such band bending as a function of ETL thickness, we conducted additional UPS/LE-IPES measurements (fig. S6 and S7) that allowed us to map out the band structure at the perovskite/ETL interface. The perovskite/C₆₀ sample displayed negligible band bending (fig. S6), which is consistent with previous work on the MAPbI₃/C₆₀ interface (31). However, the presence of a MgF_x interlayer led to energy band bending at the perovskite surface (Fig. 1D). Also, the lowest unoccupied molecular orbital (LUMO) of the C₆₀ layer bent down toward the perovskite interface, which implied that the MgF_x layer promoted the formation of electron-selective contacts with low interfacial resistance (32).

Moreover, the MgF_x interlayer also displaced C₆₀ from the perovskite surface, thus suppressing interface recombination (see below). The thinness of the metal fluoride interlayer with a thickness of 0.5~1.5 nm ensures that collected electrons can reach the LUMO of the C₆₀ layer through

quantum-mechanical tunneling or via pinholes, thus enabling the selective extraction of electrons. Once the electrons transferred to C₆₀, they became the majority charge carriers and were easily transported through the C₆₀ layer and collected by the SnO₂/IZO transparent electrode. Furthermore, X-ray photoelectron spectroscopy (XPS) results (fig. S8) showed that the evaporated ultrathin (~1 nm) MgF_x films strongly deviated from their bulk stoichiometric (*x*=2) composition, with an *x* value in the range 1.0 ± 0.2. We expect this substoichiometric nature to produce a transverse electric dipole in this layer that promotes electron extraction.

To evaluate enhanced contact passivation with fluoride interlayers, we quantified the non-radiative recombination losses at the perovskite/ETL interfaces through absolute photoluminescence (PL) imaging under 1-sun equivalent illumination. This method let us extract the quasi-Fermi-level splitting (*QFLS* or Δμ) in the perovskite layer, which relates to the upper voltage limit of complete devices (33, 34). Figure 2A and fig. S9 showed that the mean *QFLS* of IZO/2PACz/perovskite structures without ETL was ~1.285 eV, whereas the IZO/2PACz/perovskite/C₆₀ sample exhibited a sharp decline of *QFLS* with a mean value of 1.179 eV. The LiF- and MgF_x-treated samples display *QFLS* values of 1.198 and 1.217 eV, respectively. The HTL side remained unchanged, so we associated the undesired lower *QFLS* with trap-assisted recombination at the perovskite/ETL interface. Structural disorder or molecular imperfections in fullerene-based ETLs commonly have a strong band tail state (35, 36) that may interact electronically with the perovskite layer to form undesired recombination channels.

Time-resolved photoluminescence (TRPL) spectroscopy further revealed that the IZO/2PACz/perovskite structure supported a very slow carrier decay process with an average carrier lifetime of ~1.6 μs (Fig. 2B and table S1). Coating C₆₀ directly onto the perovskite expectedly caused a large reduction in PL lifetime to 26 ns, but the use of a MgF_x interlayer prolonged the average PL decay time to 83 ns, compared to 38 ns for the perovskite/C₆₀ sample.

Transient absorption spectroscopy (TAS, see fig. S11) revealed a sharp negative band peaking at 718 and 710 nm for bare and C₆₀-coated perovskite samples, respectively, that could be assigned to ground-state photobleaching. As expected, the TAS signals of the perovskite/C₆₀ sample exhibited faster decay of the bleaching peak than their perovskite/MgF_x/C₆₀ counterparts. By globally fitting the TA decay curves of the three samples under four laser excitation conditions to a diffusion equation (fig. S10), we obtained a first-order charge-carrier decay constant *k*₁ of 3.48×10⁵ s⁻¹ (1/*k*₁≈2.87 μs). This value was consistent with our PL decay and the electron-hole diffusion length of ~12 μm, which is much longer than perovskite thickness, as desired for efficient solar cells.

These results indicate that the trap states causing nonradiative recombination mainly reside at the perovskite/ETL interface. To investigate the origin of these traps, we conducted density functional theory (DFT) calculations with the structural model of the perovskite/C₆₀ interface shown in Fig. 2C. The density of states (DOS) calculated at the relaxed contact distance showed the formation of deep trap states within the perovskite bandgap (inset, Fig. 2C). Similar calculations on prototypical FAPbI₃ perovskite confirmed the formation of such induced states (fig. S12). Notably, these states are not created by defects in the perovskite but are induced by proximity with C₆₀ and are similar to metal-induced gap states in metal/semiconductor contacts (37, 38). The MgF_x interlayer displaced C₆₀ away from the perovskite and suppressed the induced trap states. Based on these findings, we argue that a key role of the interlayers is the blocking of the gap-state assisted recombination channels, thus suppressing charge recombination at the perovskite/ETL interface. In addition, DFT calculations showed that without interlayers, partial electron transfer from the perovskite into the C₆₀ (fig. S16) created a barrier for electron extraction.

To verify improved charge extraction at the perovskite/C₆₀ interface, we fabricated single-junction *p-i-n* devices with metal fluoride-based interlayers, as well as control samples without interlayer. The solar cell with a MgF_x contact displacer reached a V_{oc} of 1.23 V, representing a ~50 mV absolute enhancement when compared to the control (fig. S17) and a ~20 mV enhancement versus a LiF interlayer. These results agreed well with our energy-level and surface-passivation analyses. Notably, the *FF* improved to 81.1%, which we attributed to enhanced charge extraction and suppressed interface recombination at maximum-power point conditions. In addition, we tested CaF_x devices and found they also show remarkable V_{oc} and *FF*, implying that the alkali-earth metal fluoride as a contact displacer is a generic route to improve device performance.

We fabricated monolithic perovskite/silicon tandem solar cells using double-textured Si bottom cell with a sub-micrometer random pyramid structure (fig. S19). The MgF_x-based device showed a remarkable reverse-scan *PCE* of up to 30.5% with a short-circuit current density, J_{sc} of 19.8 mA/cm², a V_{oc} of 1.92 V, and a *FF* of 80.7% (Fig. 3A). The control tandem showed a best *PCE* of 28.6% with a J_{sc} of 19.8 mA/cm², a V_{oc} of 1.85 V, an *FF* of 77.9% under reverse scan. The device statistics (Fig. 3, B and C, and fig. S20) corroborated that the *PCE* improvement was mainly the result of enhanced V_{oc} and *FF*. One unencapsulated MgF_x-based tandem was certified at Fraunhofer ISE CaLab, showed a reverse-scan *PCE* of 29.4% with a J_{sc} of 19.8 mA/cm², a V_{oc} of 1.91 V, an *FF* of 77.6%, and a steady-state *PCE* of 29.3% (Fig. 3D and fig. S21). Integrating the calibrated *EQE* (Fig. 3E) over the AM1.5G spectrum yielded J_{sc} values of 20.0 and 19.8

mA/cm² for the perovskite and c-Si subcells, respectively, which agreed with our tandem J_{sc} values of ~19.8 mA/cm². Our optical analysis revealed that the optical loss, in addition to some reflection, mainly came from parasitic absorption in the IZO transparent top electrode and C₆₀ layer (fig. S22), which accounted for equivalent values of 0.64 and 0.62 mA/cm², respectively.

To evaluate the perovskite subcell device performance, we conducted electroluminescence (EL) measurements on tandem devices. With an injected current density of 22 mA/cm², we observed well-resolved EL spectral mapping with peaks positioning at ~735 nm (Fig. 3, F and G), corresponding to the perovskite bandgap energy of ~1.69 eV. Under any current injection condition, the MgF_x-based tandem showed a relatively higher EL emission intensity than the control device, indicating a higher internal voltage (fig. S24). Combining the EL spectra results of the perovskite subcell under distinct current injection conditions with Suns- V_{oc} data of the c-Si single-junction cell, we constructed so-called pseudo *J-V* curves of our perovskite/silicon tandem (Fig. 3H), free of any series resistance (R_s) losses. For the MgF_x-based tandem, we obtained a pseudo- V_{oc} of 1.93 V which is remarkably near the V_{oc} of 1.92 V from standard *J-V* measurements. A pseudo-*FF* of 84.8% and pseudo-*PCE* of 32.5% could be also estimated, implying that ~3% in absolute *PCE* was lost to series resistance.

We explored the effect of the interlayer on device stability by monitoring the photovoltaic performance of the control and fluoride-based tandems without encapsulation under continual standard AM1.5G illumination (Fig. 4A). The control device benefitted from light soaking in that its *PCE* increased from initially 27.2% to 28.0% after 10 min of illumination. The *J-V* curves (fig. S26) demonstrated that the light soaking improved V_{oc} and *FF*; we speculate that continuous illumination caused a slight favorable adjustment of the energy alignment at the perovskite/ETL interface. The fluoride-based devices did not appear to benefit from this (Fig. 4B and fig. S26), possibly because of the improved energy-level alignment at their perovskite/ETL interface. On a longer timescale, the LiF-based tandem, reputed for low stability (19), showed a gradual performance drop from 29.1% to 27.5% in air, whereas the MgF_x-based tandem retained nearly >99% of its initial *PCE* after 260 min, which we attribute to MgF_x being non-hygroscopic and having a lower metal ion diffusivity. The control device maintained relatively stable, but still lower absolute V_{oc} and *FF* values after the light-soaking period, compared to MgF_x-based devices.

In addition, we subjected our encapsulated tandem device to damp-heat testing (85°C with 85% relative humidity, RH, IEC 61215:2021 standard, Fig. 4C and fig. S27). The MgF_x-treated tandem device did not show any V_{oc} or J_{sc} deg-

radiation after over 1000 hours, and retained 95.4% of its initial *PCE*. The V_{oc} even improved slightly, indicating that the perovskite itself and the interfacial layers were sufficiently tolerant to thermal stress. The *FF* showed a slight drop, which may be related to the increase in the series resistance of the contact electrode. In contrast, the LiF-treated tandem showed an obvious drop in *PCE* after an initial 125-hour testing (Fig. 4C and fig. S27). These results indicated that our MgF_2 -tandem devices, with a reasonable encapsulation scheme, could pass the damp-heat test protocol of the IEC 61215:2021 standard.

REFERENCES AND NOTES

1. T. Leijtens, K. A. Bush, R. Prasanna, M. D. McGehee, Opportunities and challenges for tandem solar cells using metal halide perovskite semiconductors. *Nat. Energy* **3**, 828–838 (2018). [doi:10.1038/s41560-018-0190-4](https://doi.org/10.1038/s41560-018-0190-4)
2. R. Wang, T. Huang, J. Xue, J. Tong, K. Zhu, Y. Yang, Prospects for metal halide perovskite-based tandem solar cells. *Nat. Photonics* **15**, 411–425 (2021). [doi:10.1038/s41566-021-00809-8](https://doi.org/10.1038/s41566-021-00809-8)
3. H. Shen, S. T. Omelchenko, D. A. Jacobs, S. Yalamanchili, Y. Wan, D. Yan, P. Phang, T. Duong, Y. Wu, Y. Yin, C. Samundsett, J. Peng, N. Wu, T. P. White, G. G. Andersson, N. S. Lewis, K. R. Catchpole, In situ recombination junction between p-Si and TiO_2 enables high-efficiency monolithic perovskite/Si tandem cells. *Sci. Adv.* **4**, eaau9711 (2018). [doi:10.1126/sciadv.aau9711](https://doi.org/10.1126/sciadv.aau9711) [Medline](#)
4. E. Aydin, J. Liu, E. Ugur, R. Azmi, G. T. Harrison, Y. Hou, B. Chen, S. Zhumagali, M. De Bastiani, M. C. Wang, W. Raja, T. G. Allen, A. U. Rehman, A. S. Subbiah, M. Babics, A. Babayigit, F. H. Isikgor, K. Wang, E. Van Kerschaver, L. Tsetseris, E. H. Sargent, F. Laquai, S. De Wolf, Ligand-bridged charge extraction and enhanced quantum efficiency enable efficient n-i-p perovskite/silicon tandem solar cells. *Energy Environ. Sci.* **14**, 4377–4390 (2021). [doi:10.1039/D1EE01206A](https://doi.org/10.1039/D1EE01206A)
5. A. Richter, M. Hermle, S. W. Glunz, Reassessment of the Limiting Efficiency for Crystalline Silicon Solar Cells. *IEEE Int. J. Photovolt.* **3**, 1184–1191 (2013). [doi:10.1109/JPHOTOV.2013.2270351](https://doi.org/10.1109/JPHOTOV.2013.2270351)
6. B. Chen, Z. Yu, K. Liu, X. Zheng, Y. Liu, J. Shi, D. Spronk, P. N. Rudd, Z. Holman, J. Huang, Grain Engineering for Perovskite/Silicon Monolithic Tandem Solar Cells with Efficiency of 25.4%. *Joule* **3**, 177–190 (2019). [doi:10.1016/j.joule.2018.10.003](https://doi.org/10.1016/j.joule.2018.10.003)
7. J. P. Mailoa, C. D. Bailie, E. C. Johlin, E. T. Hoke, A. J. Akey, W. H. Nguyen, M. D. McGehee, T. Buonassisi, A 2-terminal perovskite/silicon multijunction solar cell enabled by a silicon tunnel junction. *Appl. Phys. Lett.* **106**, 121105 (2015). [doi:10.1063/1.4914179](https://doi.org/10.1063/1.4914179)
8. B. Chen, Z. S. J. Yu, S. Manzoor, S. Wang, W. Weigand, Z. H. Yu, G. Yang, Z. Y. Ni, X. Z. Dai, Z. C. Holman, J. S. Huang, Blade-Coated Perovskites on Textured Silicon for 26%-Efficient Monolithic Perovskite/Silicon Tandem Solar Cells. *Joule* **4**, 850–864 (2020). [doi:10.1016/j.joule.2020.01.008](https://doi.org/10.1016/j.joule.2020.01.008)
9. J. Liu, E. Aydin, J. Yin, M. De Bastiani, F. H. Isikgor, A. U. Rehman, E. Yengel, E. Ugur, G. T. Harrison, M. Wang, Y. Gao, J. I. Khan, M. Babics, T. G. Allen, A. S. Subbiah, K. Zhu, X. Zheng, W. Yan, F. Xu, M. F. Salvador, O. M. Bakr, T. D. Anthopoulos, M. Lanza, O. F. Mohammed, F. Laquai, S. De Wolf, 28.2%-efficient, outdoor-stable perovskite/silicon tandem solar cell. *Joule* **5**, 3169–3186 (2021). [doi:10.1016/j.joule.2021.11.003](https://doi.org/10.1016/j.joule.2021.11.003)
10. M. Jošt, E. Köhnen, A. B. Morales-Vilches, B. Lipovšek, K. Jäger, B. Macco, A. Al-Ashouri, J. Krč, L. Korte, B. Rech, R. Schlatmann, M. Topič, B. Stannowski, S. Albrecht, Textured interfaces in monolithic perovskite/silicon tandem solar cells: Advanced light management for improved efficiency and energy yield. *Energy Environ. Sci.* **11**, 3511–3523 (2018). [doi:10.1039/C8EE02469C](https://doi.org/10.1039/C8EE02469C)
11. F. Sahli, J. Werner, B. A. Kamino, M. Bräuninger, R. Monnard, B. Paviet-Salomon, L. Barraud, D. Ding, J. J. Diaz Leon, D. Sacchetti, G. Cattaneo, M. Despeisse, M. Boccard, S. Nicolay, Q. Jeangros, B. Niesen, C. Ballif, Fully textured monolithic perovskite/silicon tandem solar cells with 25.2% power conversion efficiency. *Nat. Mater.* **17**, 820–826 (2018). [doi:10.1038/s41563-018-0115-4](https://doi.org/10.1038/s41563-018-0115-4) [Medline](#)
12. R. Santbergen, R. Mishima, T. Meguro, M. Hino, H. Uzu, J. Blanker, K. Yamamoto, M. Zeman, Minimizing optical losses in monolithic perovskite/c-Si tandem solar cells with a flat top cell. *Opt. Express* **24**, A1288–A1299 (2016). [doi:10.1364/OE.24.0A1288](https://doi.org/10.1364/OE.24.0A1288) [Medline](#)
13. K. A. Bush, A. F. Palmstrom, Z. J. Yu, M. Boccard, R. Cheacharoen, J. P. Mailoa, D. P. McMeekin, R. L. Z. Hoyer, C. D. Bailie, T. Leijtens, I. M. Peters, M. C. Minichetti, N. Rolston, R. Prasanna, S. Sofia, D. Harwood, W. Ma, F. Moghadam, H. J. Snath, T. Buonassisi, Z. C. Holman, S. F. Bent, M. D. McGehee, 23.6%-efficient monolithic perovskite/silicon tandem solar cells with improved stability. *Nat. Energy* **2**, 17009 (2017). [doi:10.1038/nenergy.2017.9](https://doi.org/10.1038/nenergy.2017.9)
14. D. Kim, H. J. Jung, I. J. Park, B. W. Larson, S. P. Dunfield, C. Xiao, J. Kim, J. Tong, P. Boonmongkolras, S. G. Ji, F. Zhang, S. R. Pae, M. Kim, S. B. Kang, V. David, J. J. Berry, J. Y. Kim, K. Zhu, D. H. Kim, B. Shin, Efficient, stable silicon tandem cells enabled by anion-engineered wide-bandgap perovskites. *Science* **368**, 155–160 (2020). [doi:10.1126/science.aba3433](https://doi.org/10.1126/science.aba3433) [Medline](#)
15. J. Xu, C. C. Boyd, Z. J. Yu, A. F. Palmstrom, D. J. Witter, B. W. Larson, R. M. France, J. Werner, S. P. Harvey, E. J. Wolf, W. Weigand, S. Manzoor, M. F. A. M. van Hest, J. J. Berry, J. M. Luther, Z. C. Holman, M. D. McGehee, Triple-halide wide-band gap perovskites with suppressed phase segregation for efficient tandems. *Science* **367**, 1097–1104 (2020). [doi:10.1126/science.aaz5074](https://doi.org/10.1126/science.aaz5074) [Medline](#)
16. Y. Hou, E. Aydin, M. De Bastiani, C. Xiao, F. H. Isikgor, D.-J. Xue, B. Chen, H. Chen, B. Bahrami, A. H. Chowdhury, A. Johnston, S.-W. Baek, Z. Huang, M. Wei, Y. Dong, J. Troughton, R. Jalmood, A. J. Mirabelli, T. G. Allen, E. Van Kerschaver, M. I. Saidaminov, D. Baran, Q. Qiao, K. Zhu, S. De Wolf, E. H. Sargent, Efficient tandem solar cells with solution-processed perovskite on textured crystalline silicon. *Science* **367**, 1135–1140 (2020). [doi:10.1126/science.aaz3691](https://doi.org/10.1126/science.aaz3691) [Medline](#)
17. S. Zhumagali, F. H. Isikgor, P. Maity, J. Yin, E. Ugur, M. De Bastiani, A. S. Subbiah, A. J. Mirabelli, R. Azmi, G. T. Harrison, J. Troughton, E. Aydin, J. Liu, T. Allen, A. Rehman, D. Baran, O. F. Mohammed, S. De Wolf, Linked Nickel Oxide/Perovskite Interface Passivation for High-Performance Textured Monolithic Tandem Solar Cells. *Adv. Energy Mater.* **11**, 2101662 (2021). [doi:10.1002/aenm.202101662](https://doi.org/10.1002/aenm.202101662)
18. A. Al-Ashouri, A. Magomedov, M. Roß, M. Jošt, M. Talaikis, G. Chistiakova, T. Bertram, J. A. Márquez, E. Köhnen, E. Kasparavičius, S. Levchenko, L. Gil-Escrig, C. J. Hages, R. Schlatmann, B. Rech, T. Malinauskas, T. Unold, C. A. Kaufmann, L. Korte, G. Niaura, V. Getautis, S. Albrecht, Conformal monolayer contacts with lossless interfaces for perovskite single junction and monolithic tandem solar cells. *Energy Environ. Sci.* **12**, 3356–3369 (2019). [doi:10.1039/C9EE02268F](https://doi.org/10.1039/C9EE02268F)
19. A. Al-Ashouri, E. Köhnen, B. Li, A. Magomedov, H. Hempel, P. Caprioglio, J. A. Márquez, A. B. Morales Vilches, E. Kasparavičius, J. A. Smith, N. Phung, D. Menzel, M. Grischek, L. Kegelmann, D. Skrobilin, C. Gollwitzer, T. Malinauskas, M. Jošt, G. Matič, B. Rech, R. Schlatmann, M. Topič, L. Korte, A. Abate, B. Stannowski, D. Neher, M. Stollerfoht, T. Unold, V. Getautis, S. Albrecht, Monolithic perovskite/silicon tandem solar cell with >29% efficiency by enhanced hole extraction. *Science* **370**, 1300–1309 (2020). [doi:10.1126/science.abd4016](https://doi.org/10.1126/science.abd4016) [Medline](#)
20. E. L. Unger, L. Kegelmann, K. Suchan, D. Sörell, L. Korte, S. Albrecht, Roadmap and roadblocks for the band gap tunability of metal halide perovskites. *J. Mater. Chem. A* **11**, 11401–11409 (2017). [doi:10.1039/C7TA00404D](https://doi.org/10.1039/C7TA00404D)
21. F. Peña-Camargo, P. Caprioglio, F. Zu, E. Gutierrez-Partida, C. M. Wolff, K. Brinkmann, S. Albrecht, T. Riedl, N. Koch, D. Neher, M. Stollerfoht, Halide Segregation versus Interfacial Recombination in Bromide-Rich Wide-Gap Perovskite Solar Cells. *ACS Energy Lett.* **5**, 2728–2736 (2020). [doi:10.1021/acsenenergylett.0c01104](https://doi.org/10.1021/acsenenergylett.0c01104)
22. M. Stollerfoht, P. Caprioglio, C. M. Wolff, J. A. Márquez, J. Nordmann, S. Zhang, D. Rothhardt, U. Hörmann, Y. Amir, A. Redinger, L. Kegelmann, F. Zu, S. Albrecht, N. Koch, T. Kirchartz, M. Saliba, T. Unold, D. Neher, The impact of energy alignment and interfacial recombination on the internal and external open-circuit voltage of perovskite solar cells. *Energy Environ. Sci.* **12**, 2778–2788 (2019).

- [doi:10.1039/C9FE02020A](https://doi.org/10.1039/C9FE02020A)
23. J. S. Luo, J. X. Xia, H. Yang, L. L. Chen, Z. Q. Wan, F. Han, H. A. Malik, X. H. Zhu, C. Y. Jia, Toward high-efficiency, hysteresis-less, stable perovskite solar cells: Unusual doping of a hole-transporting material using a fluorine-containing hydrophobic Lewis acid. *Energy Environ. Sci.* **11**, 2035–2045 (2018). [doi:10.1039/C8EE00036K](https://doi.org/10.1039/C8EE00036K)
 24. S.-G. Kim, T. H. Le, T. de Monfreid, F. Goubard, T.-T. Bui, N.-G. Park, Capturing Mobile Lithium Ions in a Molecular Hole Transporter Enhances the Thermal Stability of Perovskite Solar Cells. *Adv. Mater.* **33**, e2007431 (2021). [doi:10.1002/adma.202007431](https://doi.org/10.1002/adma.202007431) [Medline](#)
 25. Z. Li, C. Xiao, Y. Yang, S. P. Harvey, D. H. Kim, J. A. Christians, M. Yang, P. Schulz, S. U. Nanayakkara, C.-S. Jiang, J. M. Luther, J. J. Berry, M. C. Beard, M. M. Al-Jassim, K. Zhu, Extrinsic ion migration in perovskite solar cells. *Energy Environ. Sci.* **10**, 1234–1242 (2017). [doi:10.1039/C7EE00358G](https://doi.org/10.1039/C7EE00358G)
 26. Z. Liu, J. Siekmann, B. Klingebiel, U. Rau, T. Kirchartz, Interface Optimization via Fullerene Blends Enables Open-Circuit Voltages of 1.35 V in $\text{CH}_3\text{NH}_3\text{Pb}(\text{I}_{0.8}\text{Br}_{0.2})_3$ Solar Cells. *Adv. Energy Mater.* **11**, 2003386 (2021). [doi:10.1002/aenm.202003386](https://doi.org/10.1002/aenm.202003386)
 27. Q. Jiang, Y. Zhao, X. Zhang, X. Yang, Y. Chen, Z. Chu, Q. Ye, X. Li, Z. Yin, J. You, Surface passivation of perovskite film for efficient solar cells. *Nat. Photonics* **13**, 460–466 (2019). [doi:10.1038/s41566-019-0398-2](https://doi.org/10.1038/s41566-019-0398-2)
 28. E. Aydin, C. Altinkaya, Y. Smirnov, M. A. Yaqin, K. P. S. Zanoni, A. Paliwal, Y. Firdaus, T. G. Allen, T. D. Anthopoulos, H. J. Bolink, M. Morales-Masis, S. De Wolf, Sputtered transparent electrodes for optoelectronic devices: Induced damage and mitigation strategies. *Matter* **4**, 3549–3584 (2021). [doi:10.1016/j.matt.2021.09.021](https://doi.org/10.1016/j.matt.2021.09.021)
 29. J. Endres, D. A. Egger, M. Kulbak, R. A. Kerner, L. Zhao, S. H. Silver, G. Hodes, B. P. Rand, D. Cahen, L. Kronik, A. Kahn, Valence and Conduction Band Densities of States of Metal Halide Perovskites: A Combined Experimental-Theoretical Study. *J. Phys. Chem. Lett.* **7**, 2722–2729 (2016). [doi:10.1021/acs.jpclett.6b00946](https://doi.org/10.1021/acs.jpclett.6b00946) [Medline](#)
 30. L. Canil, T. Cramer, B. Fraboni, D. Ricciarelli, D. Meggiolaro, A. Singh, M. Liu, M. Rusu, C. M. Wolff, N. Phung, Q. Wang, D. Neher, T. Unold, P. Vivo, A. Gagliardi, F. De Angelis, A. Abate, Tuning halide perovskite energy levels. *Energy Environ. Sci.* **14**, 1429–1438 (2021). [doi:10.1039/D0EE02216K](https://doi.org/10.1039/D0EE02216K)
 31. P. Schulz, L. L. Whittaker-Brooks, B. A. MacLeod, D. C. Olson, Y.-L. Loo, A. Kahn, Electronic Level Alignment in Inverted Organometal Perovskite Solar Cells. *Adv. Mater. Interfaces* **2**, 1400532 (2015). [doi:10.1002/admi.201400532](https://doi.org/10.1002/admi.201400532)
 32. Y. Wan, C. Samundsett, J. Bullock, T. Allen, M. Hettick, D. Yan, P. Zheng, X. Zhang, J. Cui, J. McKeon, A. Javey, A. Cuevas, Magnesium Fluoride Electron-Selective Contacts for Crystalline Silicon Solar Cells. *ACS Appl. Mater. Interfaces* **8**, 14671–14677 (2016). [doi:10.1021/acsami.6b03599](https://doi.org/10.1021/acsami.6b03599) [Medline](#)
 33. D. W. deQuilettes, S. Koch, S. Burke, R. K. Paranjli, A. J. Shropshire, M. E. Ziffer, D. S. Ginger, Photoluminescence Lifetimes Exceeding 8 μs and Quantum Yields Exceeding 30% in Hybrid Perovskite Thin Films by Ligand Passivation. *ACS Energy Lett.* **1**, 438–444 (2016). [doi:10.1021/acsenenergylett.6b00236](https://doi.org/10.1021/acsenenergylett.6b00236)
 34. M. Stollerfoht, M. Grischek, P. Caprioglio, C. M. Wolff, E. Gutierrez-Partida, F. Peña-Camargo, D. Rothhardt, S. Zhang, M. Raoufi, J. Wolansky, M. Abdi-Jalebi, S. D. Stranks, S. Albrecht, T. Kirchartz, D. Neher, How To Quantify the Efficiency Potential of Neat Perovskite Films: Perovskite Semiconductors with an Implied Efficiency Exceeding 28. *Adv. Mater.* **32**, 2000080 (2020). [doi:10.1002/adma.202000080](https://doi.org/10.1002/adma.202000080) [Medline](#)
 35. F. Bussolotti, J. Yang, M. Hiramoto, T. Kaji, S. Kera, N. Ueno, Direct detection of density of gap states in C_{60} single crystals by photoemission spectroscopy. *Phys. Rev. B* **92**, 115102 (2015). [doi:10.1103/PhysRevB.92.115102](https://doi.org/10.1103/PhysRevB.92.115102)
 36. Y. Shao, Y. Yuan, J. Huang, Correlation of energy disorder and open-circuit voltage in hybrid perovskite solar cells. *Nat. Energy* **1**, 15001 (2016). [doi:10.1038/nenergy.2015.1](https://doi.org/10.1038/nenergy.2015.1)
 37. M. Sajjad, X. Yang, P. Altermatt, N. Singh, U. Schwingenschlögl, S. De Wolf, Metal-induced gap states in passivating metal/silicon contacts. *Appl. Phys. Lett.* **114**, 071601 (2019). [doi:10.1063/1.5066423](https://doi.org/10.1063/1.5066423)
 38. J. Robertson, Band offsets of wide-band-gap oxides and implications for future electronic devices. *J. Vac. Sci. Technol. B* **18**, 1785–1791 (2000). [doi:10.1116/1.591472](https://doi.org/10.1116/1.591472)
 39. S. M. Park, A. Abtahi, A. M. Boehm, K. R. Graham, Surface Ligands for Methylammonium Lead Iodide Films: Surface Coverage, Energetics, and Photovoltaic Performance. *ACS Energy Lett.* **5**, 799–806 (2020). [doi:10.1021/acsenenergylett.0c00054](https://doi.org/10.1021/acsenenergylett.0c00054)
 40. J.-P. Yang, F. Bussolotti, S. Kera, N. Ueno, Origin and role of gap states in organic semiconductor studied by UPS: As the nature of organic molecular crystals. *J. Phys. D* **50**, 423002 (2017). [doi:10.1088/1361-6463/aa840f](https://doi.org/10.1088/1361-6463/aa840f)
 41. C. A. Hoffman, K. Jarašiusas, H. J. Gerritsen, A. V. Nurmikko, Measurement of surface recombination velocity in semiconductors by diffraction from picosecond transient free-carrier gratings. *Appl. Phys. Lett.* **33**, 536–539 (1978). [doi:10.1063/1.90428](https://doi.org/10.1063/1.90428)
 42. Y. Yang, M. Yang, D. T. Moore, Y. Yan, E. M. Miller, K. Zhu, M. C. Beard, Top and bottom surfaces limit carrier lifetime in lead iodide perovskite films. *Nat. Energy* **2**, 16207 (2017). [doi:10.1038/nenergy.2016.207](https://doi.org/10.1038/nenergy.2016.207)
 43. F. Lang, E. Köhnen, J. Warby, K. Xu, M. Grischek, P. Wagner, D. Neher, L. Korte, S. Albrecht, M. Stollerfoht, Revealing Fundamental Efficiency Limits of Monolithic Perovskite/Silicon Tandem Photovoltaics through Subcell Characterization. *ACS Energy Lett.* **6**, 3982–3991 (2021). [doi:10.1021/acsenenergylett.1c01783](https://doi.org/10.1021/acsenenergylett.1c01783)
 44. F. H. Isikgor, F. Furlan, J. Liu, E. Ugur, M. K. Eswaran, A. S. Subbiah, E. Yengel, M. De Bastiani, G. T. Harrison, S. Zhumagali, C. T. Howells, E. Aydin, M. Wang, N. Gasparini, T. G. Allen, A. Rehman, E. Van Kerschaver, D. Baran, I. McCulloch, T. D. Anthopoulos, U. Schwingenschlögl, F. Laquai, S. De Wolf, Concurrent cationic and anionic perovskite defect passivation enables 27.4% perovskite/silicon tandems with suppression of halide segregation. *Joule* **5**, 1566–1586 (2021). [doi:10.1016/j.joule.2021.05.013](https://doi.org/10.1016/j.joule.2021.05.013)
 45. J. P. Perdew, K. Burke, M. Ernzerhof, Generalized Gradient Approximation Made Simple. *Phys. Rev. Lett.* **77**, 3865–3868 (1996). [doi:10.1103/PhysRevLett.77.3865](https://doi.org/10.1103/PhysRevLett.77.3865) [Medline](#)
 46. G. Kresse, D. Joubert, From ultrasoft pseudopotentials to the projector augmented-wave method. *Phys. Rev. B* **59**, 1758–1775 (1999). [doi:10.1103/PhysRevB.59.1758](https://doi.org/10.1103/PhysRevB.59.1758)
 47. A. Walsh et al., WMD-group/hybrid-perovskites: Collection 1 (v1.0). Zenodo (2019). [doi:10.5281/zenodo.2641358](https://doi.org/10.5281/zenodo.2641358)
 48. N. Li, S. Tao, Y. Chen, X. Niu, C. K. Onwudinanti, C. Hu, Z. Qiu, Z. Xu, G. Zheng, L. Wang, Y. Zhang, L. Li, H. Liu, Y. Lun, J. Hong, X. Wang, Y. Liu, H. Xie, Y. Gao, Y. Bai, S. Yang, G. Brocks, Q. Chen, H. Zhou, Cation and anion immobilization through chemical bonding enhancement with fluorides for stable halide perovskite solar cells. *Nat. Energy* **4**, 408–415 (2019). [doi:10.1038/s41560-019-0382-6](https://doi.org/10.1038/s41560-019-0382-6)
 49. S. Grimme, J. Antony, S. Ehrlich, H. Krieg, A consistent and accurate ab initio parametrization of density functional dispersion correction (DFT-D) for the 94 elements H-Pu. *J. Chem. Phys.* **132**, 154104 (2010). [doi:10.1063/1.3382344](https://doi.org/10.1063/1.3382344) [Medline](#)
 50. R. A. Jishi, O. B. Ta, A. A. Sharif, Modeling of Lead Halide Perovskites for Photovoltaic Applications. *J. Phys. Chem. C* **118**, 28344–28349 (2014). [doi:10.1021/jp5050145](https://doi.org/10.1021/jp5050145)
 51. K.-H. Chew, R. Kuwahara, K. Ohno, Electronic structure of Li^+C_{60} adsorbed on methyl-ammonium lead iodide perovskite $\text{CH}_3\text{NH}_3\text{PbI}_3$ surfaces. *Mater. Adv.* **3**, 290–299 (2022). [doi:10.1039/D1MA00741F](https://doi.org/10.1039/D1MA00741F)
 52. G. Kresse, J. Furthmüller, Efficiency of ab-initio total energy calculations for metals and semiconductors using a plane-wave basis set. *Comput. Mater. Sci.* **6**, 15–50 (1996). [doi:10.1016/0927-0256\(96\)00008-0](https://doi.org/10.1016/0927-0256(96)00008-0)
 53. K. Momma, F. Izumi, VESTA 3 for three-dimensional visualization of crystal, volumetric and morphology data. *J. Appl. Crystallogr.* **44**, 1272–1276 (2011). [doi:10.1107/S0021889811038970](https://doi.org/10.1107/S0021889811038970)
 54. A. M. Ganose, A. J. Jackson, D. O. Scanlon, sumo: Command-line tools for plotting and analysis of periodic ab initio calculations. *J. Open Source Softw.* **3**,

- 717 (2018). [doi:10.21105/joss.00717](https://doi.org/10.21105/joss.00717)
55. V. Wang, N. Xu, J.-C. Liu, G. Tang, W.-T. Geng, VASPKIT: A user-friendly interface facilitating high-throughput computing and analysis using VASP code. *Comput. Phys. Commun.* **267**, 108033 (2021). [doi:10.1016/j.cpc.2021.108033](https://doi.org/10.1016/j.cpc.2021.108033)
56. Q. Wu, S. Wu, C. I. Pakes, Impact of Surface Dipole on Resonant Electron Injection in Scanning Tunneling Spectroscopy. *Chin. J. Chem. Phys.* **26**, 393–397 (2013). [doi:10.1063/1674-0068/26/04/393-397](https://doi.org/10.1063/1674-0068/26/04/393-397)

ACKNOWLEDGMENTS

We acknowledge the use of KAUST Solar Center and Core Lab facilities and the support from its staff. **Funding:** This work was supported by the King Abdullah University of Science and Technology (KAUST) under Award No: OSR-CARF/CCF-3079, OSR-CRG2019-4093, OSR-CRG2020-4350, IED OSR-2019-4208, IED OSR-2019-4580, REI/1/4833-01-01, and OSR-CRG2018-3737. **Author contributions:** Conceptualization: JL, EA, SDW; Methodology: JL, MDB, YG, GTH, RRP, MKE, MM, AS, EA, LX; Investigation: JL, MDB, YG, GTH, RRP, MKE, MM, AS, WY, FX, LX, AuR, AR, TGA, MW, JK, AAS; Visualization: JL, GTH, RRP, MKE, MM, AS, YG, ASS, EU, MW; Funding acquisition: SDW, FL, DA, US; Supervision: SDW, FL, DA, US; Writing – original draft: JL, EA, SDW; Writing – review and editing: JL, SDW, EA, EU, MDB, FL, YG, GTH, FHI, RA. **Competing interests:** J.L. and S.D.W. are inventors on patent application (63/312,896) submitted by King Abdullah University of Science and Technology that covers the alkali-earth metal fluoride used in this work. **Data and materials availability:** All data are available in the main text or the supplementary materials. **License information:** Copyright © 2022 the authors, some rights reserved; exclusive licensee American Association for the Advancement of Science. No claim to original US government works. www.science.org/about/science-licenses-journal-article-reuse.

SUPPLEMENTARY MATERIALS

science.org/doi/10.1126/science.abn8910
 Materials and Methods
 Supplementary Text
 Figs. S1 to S27
 Table S1
 References (39–56)

Submitted 28 December 2021; resubmitted 25 March 2022
 Accepted 13 June 2022
 Published online 23 June 2022
[10.1126/science.abn8910](https://doi.org/10.1126/science.abn8910)

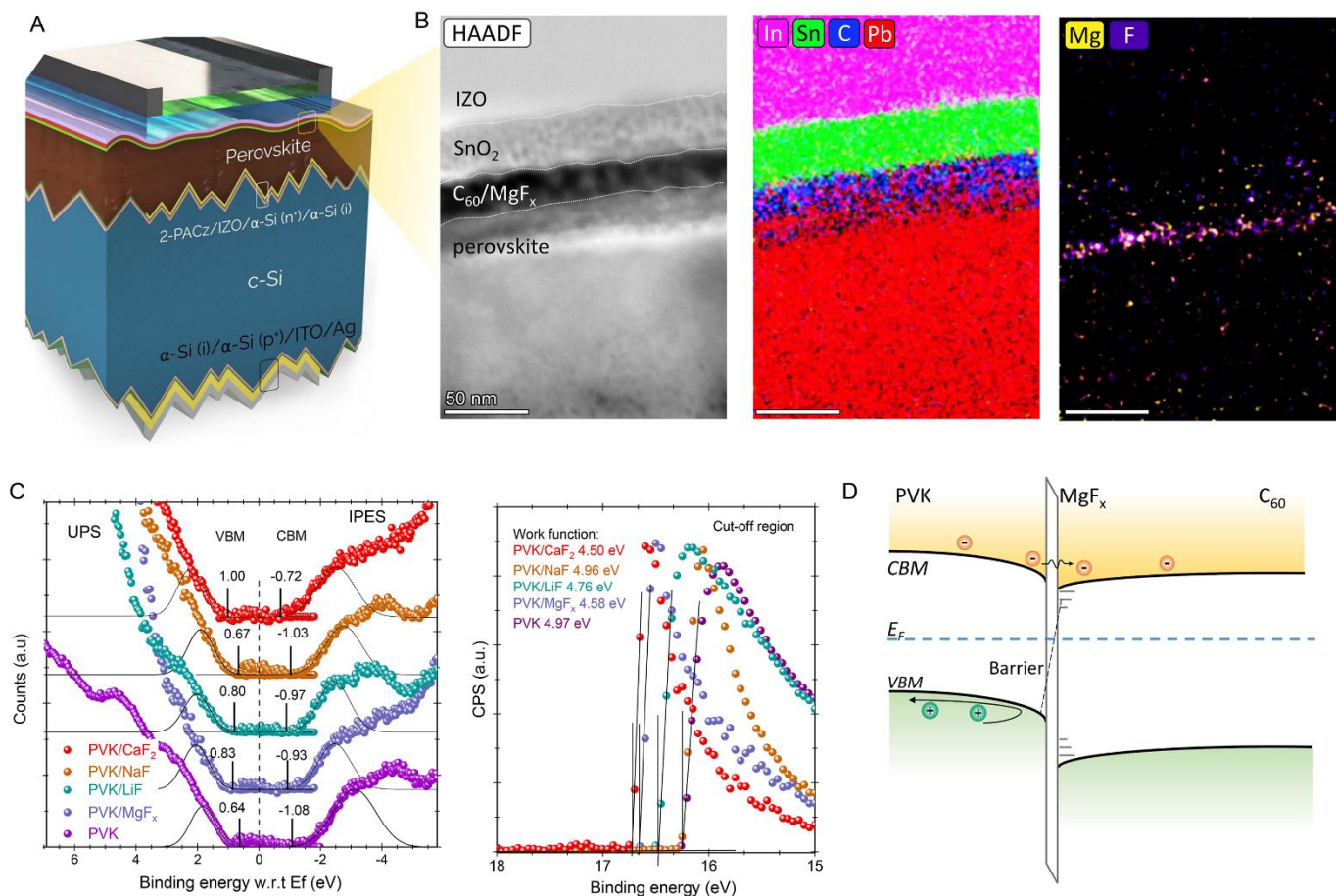


Fig. 1. Interface structure and electronic properties. (A) Schematic of the monolithic perovskite/silicon tandem solar cell built from a double-side textured silicon heterojunction cell. (B) Cross-sectional HR-STEM image and the corresponding energy-dispersive X-ray (EDX) mapping at the ETL-side. (C) Valence band (VB) and photoelectron cut-off region of the perovskite, and perovskite/1 nm-interlayer using UPS and IPES spectra. All samples were deposited on IZO/2PACz coated c-Si substrates. (D) Energy level diagram of the perovskite/ C_{60} interface with MgF_x insertion layer.

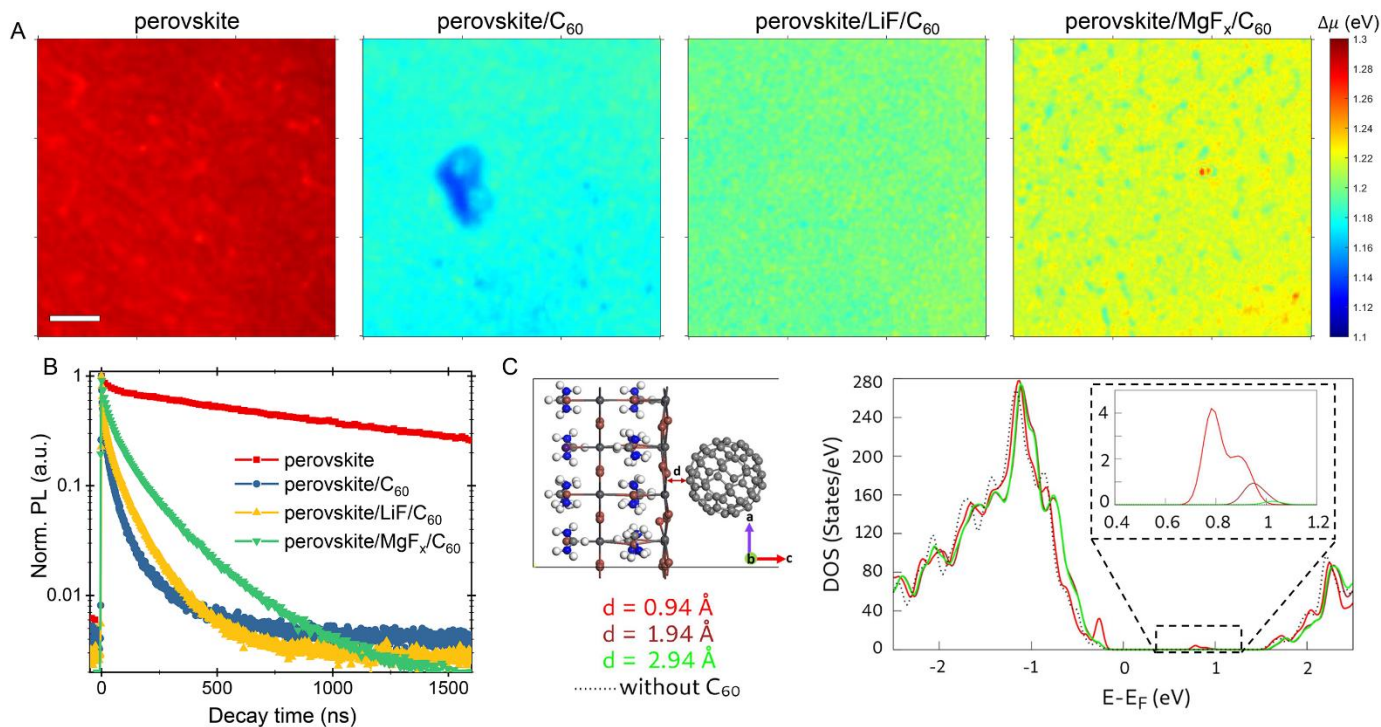


Fig. 2. Photoluminescence and transient absorption spectra. (A) Quasi-Fermi level splitting (QFLS) mapping for the perovskite, perovskite/C₆₀, perovskite/LiF/C₆₀, and perovskite/MgF_x/C₆₀ samples on 2PACz-coated Si cell under 1 sun equivalent light intensity. The scale bar is 50 μm . (B) Time-resolved photoluminescence (TRPL) spectra of the bare perovskite and the perovskite films coated with different ETL structures. (C) Schematic model and DOS of a wide-bandgap perovskite as a function of the distance d to the C₆₀ molecule. The inset of the enlarged DOS shows the induced midgap states when C₆₀ is in close proximity to perovskite.

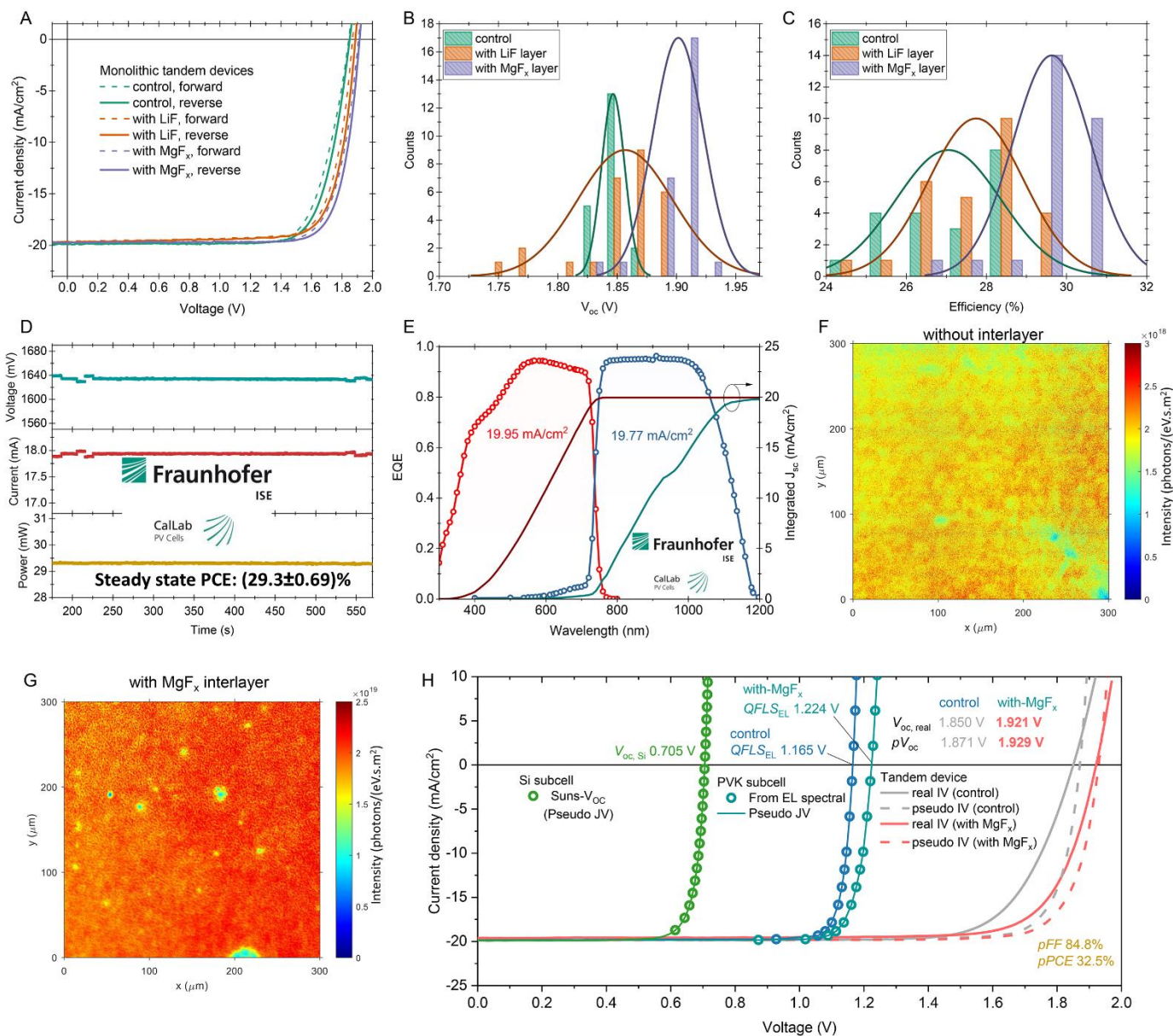


Fig. 3. Photovoltaic performances and Pseudo JV characteristics stability tests. (A) J-V curves of the champion tandem cell. (B and C) Histogram of V_{oc} (B) and PCE (C) for the tandem solar cells fabricated in this study. (D) Stabilized power output of one MgF_x -based tandem device, certified by Fraunhofer ISE Callab. (E) EQE spectra of the certified tandem device. (F and G) Absolute EL mapping of perovskite subcell without and with MgF_x interlayer under $22 \text{ mA}/\text{cm}^2$ injection current. (H) Reconstructed pseudo JV characteristics of our tandem device.

□□□

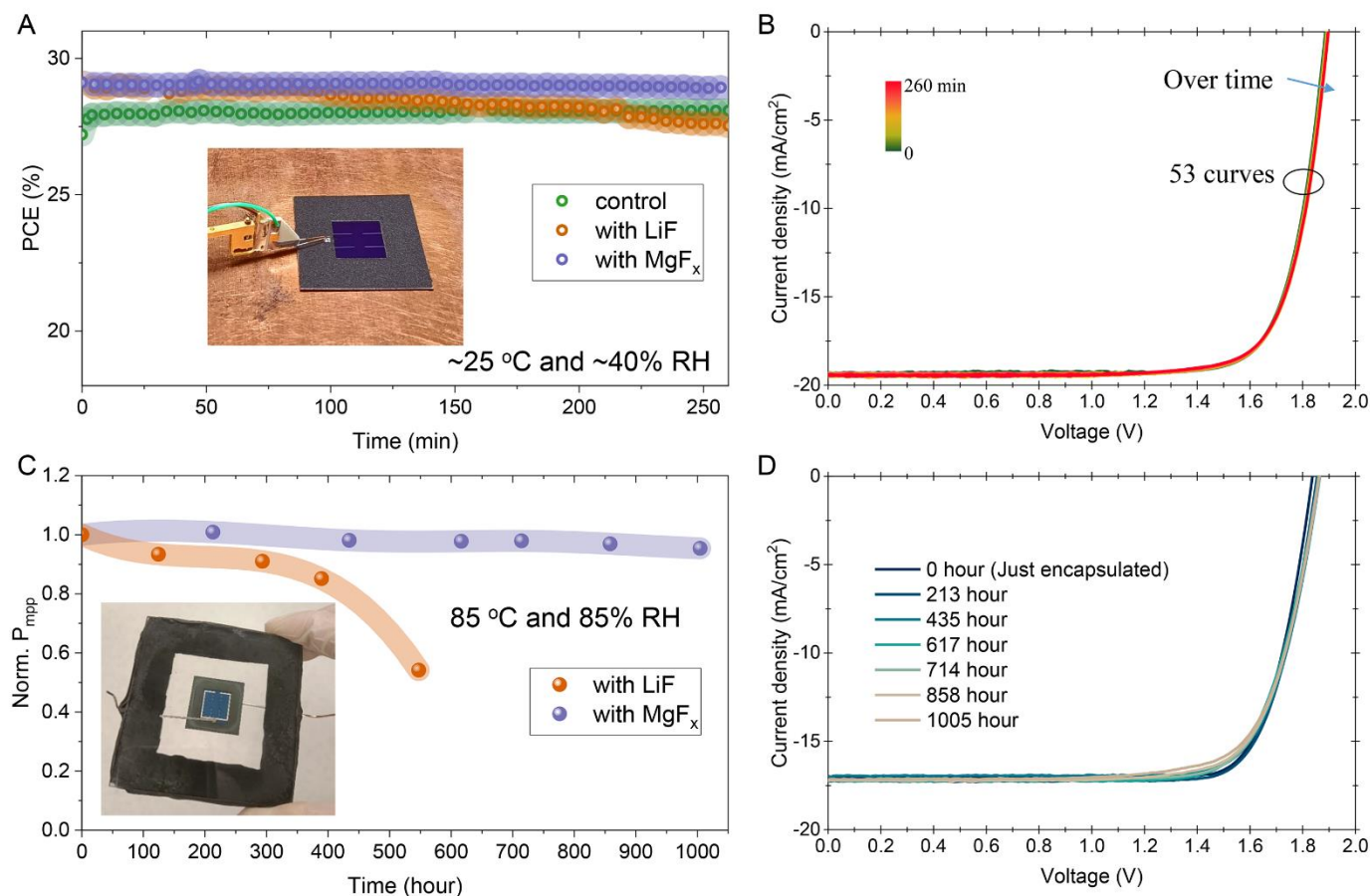


Fig. 4. Stability tests. (A) Evolution of the photovoltaic performance under continual AM 1.5G illumination for over 4 hours in air. J-V scans were performed each ~ 5 min. The inset is the photo of one device under test with a black aperture mask on it. (B) J-V curves of the tandem devices with MgF_x interlayer under continual AM 1.5G illumination. (C) Photovoltaic-performance evolution of the encapsulated tandem devices, when subjected to a damp-heat stability experiment at 85°C and 85% RH. The inset is the photo of one encapsulated device. (D) J-V curves of the tandem devices during damp heat tests.

Efficient and stable perovskite-silicon tandem solar cells through contact displacement by MgF_2

Jiang LiuMichele De BastianiErkan AydinGeorge T. HarrisonYajun GaoRakesh R. PradhanMathan K. EswaranMukunda MandalWenbo YanAkmaral SeithkanMaxime BabicsAnand S. SubbiahEsma UgurFuzong XuLujia XuMingcong WangAtteq ur RehmanArsalan RazzaqJingxuan KangRandi AzmiAhmed Ali SaidFurkan H. IsikgorThomas G. AllenDenis AndrienkoUdo SchwingenschlöglFrédéric LaquaiStefaan De Wolf

Science, Ahead of Print • DOI: 10.1126/science.abn8910

View the article online

<https://www.science.org/doi/10.1126/science.abn8910>

Permissions

<https://www.science.org/help/reprints-and-permissions>